Multiphoton Scanning Photoionization Imaging Microscopy for Single-Particle Studies of Plasmonic Metal Nanostructures

4 AUTHORS, INCLUDING:

Volker Schweikhard
Rice University
31 PUBLICATIONS **1,324** CITATIONS

Andrej Grubisic
University of Colorado at Boulder
35 PUBLICATIONS **649** CITATIONS

Multiphoton Scanning Photoionization Imaging Microscopy for Single-Particle Studies of Plasmonic Metal Nanostructures

Volker Schweikhard, Andrej Grubisic, Thomas A. Baker, and David J. Nesbitt*

JILA, University of Colorado and National Institute of Standards and Technology, and Department of Chemistry and Biochemistry, University of Colorado, Boulder, Colorado 80309-0440, United States

Photoionization studies of single Au and Ag metal nanostructures are presented, using a scanning multiphoton photoionization microscope (SPIM) with single-electron detection capability. Four-photon photoemission following ultrafast excitation at around 840 nm and two-photon photoemission following excitation at 420 nm yield high signal-to-noise 2D photoelectron images for a variety of sample materials. By way of a test demonstration of the technique, we present results obtained from SPIM imaging photolithographically patterned gold nanostructures, as well as chemically prepared crystalline gold nanorods and polycrystalline silver nanospheres. For both chemically prepared samples, striking differences in the photoemissive properties of individual nanoparticles are observed that have gone unnoticed in bulk studies. Under 840 nm excitation, for example, each Au nanorod on a Pt substrate exhibits a clear $\cos^8(\theta-\theta_0)$ dependence of photoemission strength on the angle between laser polarization (θ) and the rod axis (θ_0), suggesting that four-photon photoemission is initiated by excitation of the long-axis dipolar plasmon resonance. Surprisingly, strongly polarization-dependent photoelectron signals are also observed for nominally spherical Ag nanoparticles, albeit with varying degrees of anisotropy for different particles. AFM images of identically prepared samples reveal coverages that are consistent with those observed in SPIM images, suggesting that particle aggregation is at least not a predominant effect. One possibility consistent with the data is that localized regions of concentrated electric fields (i.e., "hot spots") or local variations of the emission propensity in these polycrystalline particles may be responsible for the polarization anisotropy, as well as dramatic temporal variations in the electron emission intensities. In summary, the studies presented here establish the SPIM technique as a new approach to exploring local electronic properties of individual metallic nanostructures.

I. Introduction

One of the most exciting recent developments in materials science is the increased control over size, shape, and composition of chemically synthesized nanoparticles. Such nanostructures already comprise several technologically and scientifically interesting classes of materials, from semiconductor nanocrystals[1,2] to metal nanoparticles[3−12] and nanomagnets.[13,14] Metal nanoparticles, because of their large surface-to-volume ratios and their ability to act as electron reservoirs, have long been recognized also as promising catalytic materials.[15,16] Only recently, they have also begun to emerge as important materials for future optoelectronics technologies[3,17−23] because of their exceptional light scattering and absorption properties as well as their ability to concentrate optical fields to deep-subwavelength volumes.[24−28] In both applications, finer aspects of the particles' size, shape, and morphology have been known to exert a crucial influence on their functionality,[11,29−37] making detailed single-particle studies essential to building up a fundamental understanding of the underlying physics.[32,37−39]

Single-particle studies present a unique opportunity for revealing heterogeneities in samples of nominally identical objects, for which bulk measurements can only reveal ensemble-averaged quantities.[40] For example, the surprising phenomenon of fluorescence blinking dynamics of colloidal semiconductor quantum dots was first identified in single-molecule experiments.[41−43] Single-molecule studies have also provided crucial information for understanding the biological functions of nominally covalently identical molecules,[44] in which kinetic heterogeneity can arise from different folding configurations or ligand binding events. To date, the vast majority of single-particle studies have relied on optical detection, such as fluorescence,[45] elastic,[46,47] or inelastic (Raman) light scattering.[48] In a few favorable cases, even single-particle absorption measurements have been possible.[49−51]

Spatial resolution in each of these techniques is constrained by the diffraction limit. In recent years, a major advance in optical imaging came about when several techniques achieved subdiffraction limited resolution (i.e., "super-resolution"). These techniques rely on the fact that the electromagnetic radiation originates from a fluorophore that is much smaller than the diffraction-limited signal detected in the far-field. Consequently, the location of the fluorophore can be determined more precisely than the diffraction limit suggests by proper analysis of the obtained signal.[52,53] Of largest practical importance are techniques based on photoswitching or photoactivation of sparse subsets of molecules (PALM,[54] STORM,[55] and FPALM[56]) as well as on stimulated emission depletion in fluorophores (STED[57]). These techniques have been applied to a wide variety of particularly biological applications.[58] Furthermore, several near-field optical techniques have been successfully employed for studying metal and semiconductor nanoparticles below the diffraction limit.[59−63]

Photoionization techniques, on the other hand, yield information complementary to optical studies and hold promise for expanding the scope of single particle studies to nonfluorescent objects. Multiphoton photoemission is a very sensitive technique

that has been widely used to study bulk surfaces, surface−adsorbate systems,[64] and nanoparticles.[65] Even in the limit of surfaces sparsely covered with metal nanoparticles, plasmon-resonant enhancement of photoelectron emission can in certain cases allow ensemble-averaged photoelectron emission properties of the adsorbed particles to be studied.[66] In this way, the detailed photoemission mechanisms of femtosecond photoionization[67] and the role of plasmon excitations in photoionization have been investigated.[25−28,65,68−71] In addition, there has recently been a growing interest in developing photoionization techniques that provide spatial resolution,[25,72−74] as well as time-resolved information.[25−28,75,76] Photoelectron emission microscopy (PEEM) has been used successfully to image patterned metal films and metal clusters,[73] as well as to reveal spatial profiles of plasmon modes in metal nanowires[77] and fractal metal nanostructures.[78] Locally enhanced photoemission in PEEM images can be used to map the local near-field distributions,[79] as demonstrated on crescent-shaped silver nanostructures. Powerful interferometric pump−probe photoemission microscopy techniques have been developed and exploited, for example, to study the dynamics of localized surface plasmon modes on silver gratings.[25] However, the level of sophisticated electron optics makes PEEM particularly challenging to implement, as well as vulnerable to signal distortion associated with charged-particle imaging. Such distortions may arise in particular due to sample charging or the presence of spatially inhomogeneous electric fields in the vicinity of metal nanoparticles and sharp metal tips.[73]

In this work, we present a comparatively simple, complementary single-particle technique based on (i) spatially resolved photoionization and (ii) single-electron detection sensitivity. It allows diffraction-limited images of a sample's local multiphoton photoelectron emissivity to be acquired. The technique capitalizes on two advantages of photoionization: (1) the naturally high sensitivity of charged-particle detection, combined with an optically nonlinear excitation mechanism that yields high spatial resolution, and (2) the potential for chemical selectivity via various resonance-enhanced multiphoton excitation pathways.

II. Setup and Materials

The basic experimental technique of scanning photoionization microscopy has been described previously.[74] In this article, major improvements to the setup are described, specifically those pertaining to the implementation of *multi*photon photoemission and single-electron detection. Both additions enhance the flexibility and sensitivity of the technique, thus allowing single metal nanoparticles to be studied. A schematic of the upgraded setup is shown in Figure 1.

II.A. Scanning Photoionization Microscopy (SPIM). Multiphoton photoemission is initiated in a near-diffraction limited ultrafast laser spot, generated by overfilling the back aperture of a reflective microscope objective in vacuo (numerical aperture, NA = 0.65). Images of local photoelectron emissivity are acquired by scanning the sample across a stationary focal spot of the excitation laser. In addition to photoelectron detection, the setup allows for observation of photons in a confocal microscope geometry, which can be employed to correlate the electronic and optical properties of nanomaterials in future studies. The output from an 85 MHz mode-locked Ti: sapphire laser serves as the excitation light source. We use either spectrally relatively narrow "red" light (840 nm with full-width-at-half-maximum (FWHM) value of 24 nm) corresponding to a Fourier-transform-limited pulse duration of 43 fs or the second harmonic of the Ti:sapphire output, "blue" light (420 nm with
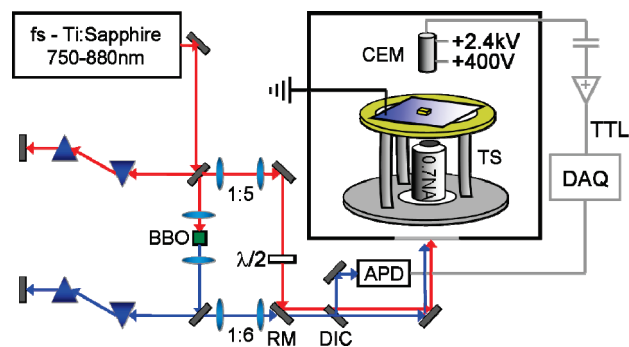

Figure 1. SPIM setup. Multiphoton photoemission is initiated in a diffraction-limited laser excitation in vacuo, yielding an image of local photoelectron emissivity by scanning the sample using piezoelectric transducers. The fundamental "red" light (tuning range 750−880 nm) or optionally doubled "blue" (tuning range 380−440 nm) light from a femtosecond Ti:sapphire laser is used for excitation with external prism pairs compressing pulses nearly to their Fourier transform limit (∼40 fs) in the sample focal plane. Electrons are detected using either a Faraday cup and a picoammeter or a Channeltron electron multiplier (CEM), amplifier/discriminator, and a 20 MHz counter.

FWHM = 6.5 nm corresponding to a Fourier-transform-limited pulse width of 40 fs). External prism compensators for both the blue and the red light provide nearly Fourier-transform-limited pulses at the focal spot on the sample ($\tau_P \approx 50$ fs). For both blue and red light, the prism separation and insertion are optimized by maximizing the photoelectron yield from a uniform 3 nm thick platinum film. Neither a single "blue" nor "red" photon supplies enough energy to photoemit electrons from materials with a typical work function $\Phi \approx 5$ eV. Instead, photoelectrons are emitted by a multiphoton process, where the required minimum number of photons n, with energy E_{photon}, is given by the threshold condition, $nE_{photon} \geq \Phi$.

Although the excitation conditions vary somewhat between the different samples examined and laser wavelengths employed, in typical conditions under 840 nm illumination the energy per laser pulse is $E_P \approx 0.4$ pJ, corresponding to ∼1.7×10^6 "red" photons per pulse. Pulses are focused to a diffraction-limited spot area $A_{spot} = 1.2025 \times FWHM^2 = 7.5 \times 10^{-9}$ cm^2, where FWHM = 0.515 λ/NA (λ = 840 nm and NA = 0.65). If we assume a nearly Fourier-transform-limited pulse width ($\tau_P \approx$ 50 fs), the peak pulse intensity is $I_P \approx 1.1 \times 10^9$ W/cm^2, with a time-averaged intensity $I_{AV} \approx 4.7$ kW/cm^2. Despite these relatively weak laser pulse conditions, about 100 e$^-$/s (electrons per second) can be optimally detected from gold nanorods (see below), which can be compared with a background of 0.5 e$^-$/s from 3 nm thick platinum films.

II.B. Electron Detection. Electrons are detected using either a Faraday cup or a Channeltron electron multiplier. In the initial experiments described herein, the Faraday cup is placed approximately 5 mm above the sample. The sample is grounded, while a +10 V bias is maintained on the Faraday cup. We have verified that at +10 V the measured SPIM current is independent of any further increase in voltage (i.e., saturated), indicating that effectively all the emitted electrons are collected. The photocurrent is measured by a picoammeter and digitized using an analog-to-digital converter.

To achieve single-electron counting sensitivity, a Channeltron electron multiplier (Photonis Magnum CEM 5901) has been installed, replacing the Faraday cup.[80] The quantum efficiency of a Channeltron detector is typically 90% for electrons with approximately 400 eV of kinetic energy and drops off dramatically for electrons with kinetic energy of <50−100 eV. Thus, the electrons are accelerated by a 400 V bias applied between

Plasmonic Metal Nanostructures

J. Phys. Chem. C, Vol. 115, No. 1, 2011 **85**

the sample and the detector entrance to maximize the detector signal. The CEM and high-voltage electrodes are enclosed in a copper shield that prevents the photoelectrons from being diverted from the detector entrance. The amplified signal pulse (gain of $\sim 10^7$ at the operating voltage of 2 kV) is fed to an amplifier/discriminator (Advanced Research Instruments) and registered by a 20 MHz counter, with an essentially background free dark count rate of ~ 0.03 e$^-$/s.

Comparison of the photocurrents from platinum films (see below), measured by the Faraday cup and the CEM under identical excitation conditions, yields an estimate for the CEM collection efficiency of $\sim 35\%$ when the CEM is placed vertically approximately 1 cm above the sample. In our range of excitation conditions no measurable electron signal is found to arise from either the blue or red light directly incident on the CEM in this configuration. We note that in the initial experiments, the CEM had been instead placed parallel to the sample, ~ 2 cm above it and displaced sideways by ~ 2 cm. In this configuration, a maximum collection efficiency of only 7% is obtained, which in addition to the bias at the detector entrance requires a corresponding bias to the copper cage of $+125$ V in order to attract electrons sideways toward the detector entrance. However, this bias is not required in the much improved vertical configuration of the CEM, whereby the electrons can follow obstruction-free trajectories from the sample to the detector.

II.C. Sample Preparation. To provide transparent, conductive substrates, 3 nm thick platinum (Pt) layers were thermally evaporated onto glass coverslips (Corning No. 1 1/2). Alternatively, 10 nm thick films of indium tin oxide (ITO) cold-deposited on glass coverslips were purchased from Advanced Thin Films. For studies of microstructured gold films, 2 nm thick gold pads were photolithographically patterned on top of the Pt substrates, following the procedures described in the literature.[74]

CTAB-capped gold (Au) nanorods (45 nm length $\times$10 nm diameter) in aqueous solution were purchased from Nanopartz and used as received. The solution absorption spectrum (Figure 3a) shows the rods' long-axis dipolar plasmon resonance centered at 830 nm with a FWHM of ~ 180 nm and an ensemble-averaged peak cross section of 2×10^{-12} cm^2 per rod. The weaker transverse plasmon is centered at 510 nm, on top of a broad interband-absorption feature appearing as a tail at shorter wavelengths. Typically, 30 μL of stock solution containing 5×10^{11} Au rods per milliliter are spin-coated onto the Pt substrates at 1500 rpm and are immediately transferred into the vacuum chamber.

Silver (Ag) nanospheres of 40 nm diameter were purchased from Nanocomposix ("biopure" nanospheres in citrate-stabilized aqueous solution, concentration 3×10^{10} particles/mL). In contrast to the single-crystalline Au rods, these spheres are polycrystalline and adopt structures that may deviate from perfect spherical geometry implied from their name. The solution absorption spectrum (Figure 5a) exhibits a narrow dipolar plasmon resonance at 413 nm, with a FWHM of 66 nm, and no other discernible features in the visible/near-infrared region. From the solution absorption spectrum, an ensemble-averaged linear absorption cross section of 4.7×10^{-11} cm^2 per particle is obtained at the peak of the plasmon resonance. Note that for excitation wavelengths around 840 nm (i.e., far detuned from the plasmon resonance) the solution absorption cross section is lower by a factor of $\sim 10^3$, i.e., $\sim 5 \times 10^{-14}$ cm^2 per particle. An amount of 40 μL of diluted stock solution (1:10 dilution in deionized H$_2$O) is spin-coated onto Pt- or ITO-coated coverslips (the solution is drop-cast onto a static coverslip and then spun
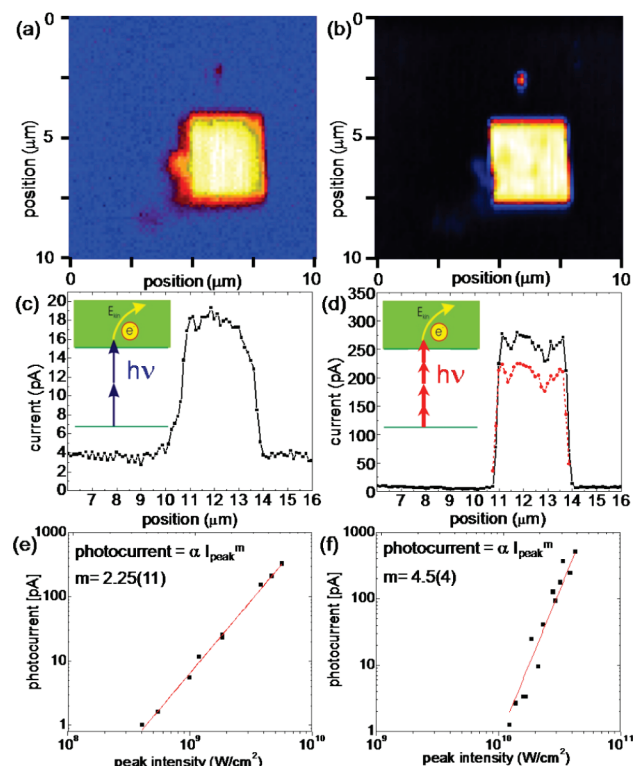

Figure 2. SPIM images of photolithographically patterned gold pads on a platinum substrate, excited with (a) blue and (b) red light. In both cases, clear contrast between the Pt substrate and the Au pads is obtained. Four-photon photoemission provides a larger signal-to-background ratio and captures features barely discernible in the two-photon photoemission image. (c, d) Lineouts through the Au pads in (a) and (b), respectively demonstrating the improved signal-to-background ratio achieved with four-photon photoemission. The dashed, red line in (d) is obtained from a repeated scan of the same sample area. Even the fine features are reproducible and represent real structure in the local photoemissivity. (e, f) The log−log plots of photocurrent from Au pads on a Faraday cup as a function of excitation intensity at 400 and 800 nm, respectively, with the slope of the data confirming the expected two-photon and four-photon dependence at 400 and 800 nm, respectively.

up to 1500 rpm). All spin-coated samples are immediately transferred into the vacuum chamber.

III. Imaging Lithographic Metal Nanostructures

The spatial imaging capability of SPIM is demonstrated by imaging two-photon photoemission under 420 nm illumination and four-photon photoemission under 840 nm excitation from micro- and nanoscale structures. To this end, SPIM images of photolithographically patterned gold pads on a platinum substrate are acquired with blue (Figure 2a and red excitation light (Figure 2b) with signals recorded using the Faraday cup detector. In both cases, a clear contrast between the Pt substrate and the Au pads is obtained. Four-photon photoemission provides a larger signal-to-background (*S/B*) ratio and captures features that are barely visible in two-photon photoemission images, such as the small spot approximately 2 μm above the gold pad visible in Figure 2b. Lineouts through the Au pad in Figure 2a and Figure 2b are plotted in Figure 2c and Figure 2d, respectively. The rise in signal (10−90%) at the edge of the gold pad occurs over a distance of 560(60) nm for 420 nm excitation, while for 840 nm excitation the rise occurs over 375(75) nm. This rise represents the convolution of the step function of the gold height profile with the multiphoton excitation profile from an Airy-

like excitation spot. From comparison with simulated step profiles, we infer laser spot sizes (FWHM of the linear intensity profile) of 690(140) nm for 840 nm excitation (i.e., within error of the diffraction limit of 650 nm) and a 760(100) nm spot for 420 nm excitation (i.e., close to but somewhat larger than the diffraction limit of 330 nm). The reason for a non-diffraction-limited 420 nm excitation spot in this image arises from slight imperfections in the spatial profile of the frequency-doubled excitation laser beam. This problem has since been remedied by further expanding the beam prior to entering the microscope objective.

The lineouts in Figure 2c and Figure 2d demonstrate the enhanced signal-to-background ratio ($S/B \approx 100{:}1$) achieved with four-photon photoemission over that with two-photon photoemission ($S/B \approx 6{:}1$). The dashed red line in Figure 2d is a lineout obtained during a repeated scan of the same sample area. It is remarkable that even the fine features in the scan are reproduced and thus represent real structure in the local photoelectron emissivity of these gold pads. Note the photoinduced reduction in photocurrent ($\sim$15%) for the rescan. At such high laser intensity, enough energy is absorbed during each pulse to heat the material within the laser focus close to the melting temperature of gold. We suspect that the strong laser intensity levels (8×10^{10} W/cm^2) employed to demonstrate the high signal-to-background ratio between gold and platinum using the relatively insensitive Faraday cup detector may cause laser-induced local smoothing of the initially rough gold surface and thus a reduction in photoelectron yield. Such photoinduced surface modifications do not, however, represent any limitation on the technique. Because of the single-electron sensitive Channeltron detector used in the subsequent experiments, excitation intensities typically 2−3 orders of magnitude lower can be employed, thus avoiding any significant laser-induced surface modifications. Photocurrent from Au pads measured as a function of excitation intensity at 400 and 800 nm is plotted in Figure 2e and Figure 2f, respectively. The slope in the plots corresponds to the order of the photoemission process and confirms that the photoemission from gold is a two-photon process at 400 nm and a four-photon process at 800 nm.

IV. Photoemission from Single Gold Nanorods Excited near Their Plasmon Resonance

To demonstrate the single-nanoparticle sensitivity of SPIM, the CEM detector was installed, and photoelectron images of a collection of gold nanorods on 3 nm thick Pt substrate were acquired by using linearly polarized, 820 nm excitation light. This wavelength is near the particles' long axis dipolar plasmon resonance in aqueous solution (see Figure 3a); hence, a plasmon-enhanced, strongly orientation-dependent response may be expected. A photoelectron image of a $24 \times 24~\mu m^2$ area of the Au rod sample on ITO is shown in Figure 3b with the indicated area shown in magnified in Figure 3c. A comparable density of spots in SPIM images and the coverage seen in AFM images of identically prepared samples suggest that the spots in SPIM arise because of emission from individual Au rods rather than their aggregates. A lineout of the scan through a sample gold nanorod (Figure 3d) demonstrates the *diffraction-limited* four-photon photoemission signal. The average width of the photoelectron signals from all rods in Figure 3b is FWHM$_4$ = 345(45) nm, where the subscript refers to the fourth order photoemission process (the order of the photoemission process was verified by observing a fourth-order dependence of photoemission signal from individual Au nanorods on the excitation laser's intensity).[84] For a photoemission process of order m the spot width
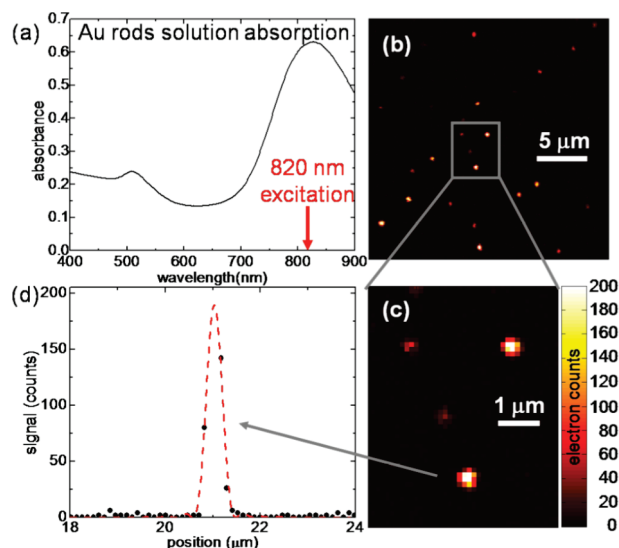

Figure 3. (a) Solution absorption spectrum of 45 nm × 10 nm Au rods exhibits the long-axis dipolar plasmon resonance at 830 nm and the weaker transverse resonance at 510 nm. (b) Multiphoton photoemission image ($24 \times 24~\mu m^2$ scan area) of a collection of gold nanorods on 2 nm thick Pt substrate under 820 nm laser illumination, where each bright spot corresponds to a single Au nanorod. Intensity differences between the rods arise mainly due to a random, noncollinear orientation of rods with respect to the linear laser polarization. (c) Magnification of the highlighted area in (b). (d) Lineout of a scan through the indicated (gray arrow) gold nanorod (data points, 340 nm FWHM). The theoretical diffraction limited fourth-order emission profile expected for 820 nm excitation light is shown in red (FWHM = 325 nm). In this and the remaining set of figures, electrons are detected using a Channeltron electron multiplier (CEM).

is given by FWHM$_m$ = FWHM$_1/\sqrt{m}$, where FWHM$_1$ is the FWHM of the excitation laser's intensity profile (i.e., Airy pattern). In the case of $\lambda = 820$ nm and objective's NA = 0.65 the diffraction-limited FWHM$_1$ = 0.515 λ/NA = 650 nm. Thus, the diffraction-limited width for a four-photon photoemission signal is calculated to be FWHM$_4$ = 325 nm, within experimental error of the measured value.

Large differences in photoemission intensity between different rods are observed in Figure 3 for a fixed linear polarization of the excitation light. With our measurement sensitivity limited by the signal-to-background ratio for Au rods on Pt, the intensities differ by as much as 2 orders of magnitude among particles. Such a large range may intuitively be expected to arise because of differences in excitation efficiency of the long-axis dipolar plasmon for rods with different random orientations with respect to the laser polarization. To investigate this possibility, a series of scans was recorded at different linear polarizations of the laser. Figure 4 shows a typical measured polarization dependence of photoemission from individual Au rods. Photoemission from Au rods on Pt is found to obey a $\cos^8(\theta - \theta_0)$ dependence on the laser's polarization angle θ, consistent with a fourth order photoemission process from a purely dipolar source, where the dipole is oriented at some random angle θ_0 (e.g., orientation of the rods' long axis). For angles that are more than 60° off-axis, photoemission is dominated by the Pt substrate. This behavior was observed consistently for all studied gold nanorods, suggesting that photoemission is indeed initiated by excitation of the gold rods' long-axis dipolar plasmon and/or enhanced by the concentrated electric fields at the rods' tips. In contrast to the large rod-to-rod variations in photoemission strength at a fixed linear polarization (Figure 7a), their peak photoemissivity (i.e., photoemission strength at a laser polariza-
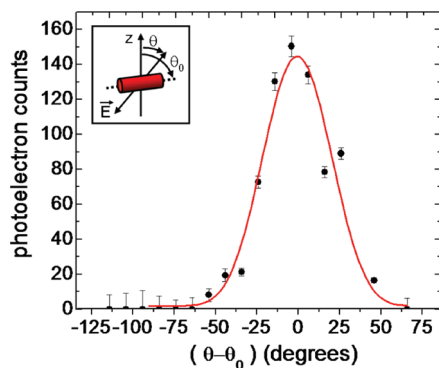
Figure 4. Polarization dependence of photoelectron emission from Au rods on Pt. The observed $\cos^8(\theta - \theta_0)$ dependence of photoemission suggests that the underlying process is a fourth order photoemission from a dipolar source, consistent with emission being initiated by excitation of the Au rod long-axis dipolar plasmon.

Figure 5. (a) Solution absorption spectrum of 40 nm diameter Ag spheres with the dominant dipolar plasmon resonance located at 413 nm. (b, c) Logarithmic SPIM images of silver nanoparticles on 3 nm thick Pt substrate and 10 nm thick ITO, respectively, excited with linearly polarized light at 830 nm. The ITO substrate exhibits a significantly lower photoionization background, revealing a coverage with Ag nanospheres that is consistent with that observed from AFM images of identically prepared samples. In contrast, the higher background from the Pt substrate (b) masks the emission from weaker particles, leading to a lower signal-to-background ratio and a lower apparent coverage. (d) Logarithmic plot of photoemission from Ag particles on ITO as a function of laser intensity.

tion angle that corresponds to that particular rod's θ_0) varies only by a factor of ∼10 (Figure 7b). This is a remarkably small factor, given the likely, high sensitivity of a fourth order photoemission process on the strength of the local electric field surrounding the emitter, thus confirming the high degree of homogeneity among the Au rods.

Au nanorods occupy only a tiny fraction ($A_{rod}/A_{spot} \approx 10^{-3}$) of the diffraction-limited excitation spot. The mere fact that they are distinguishable from the Pt substrate indicates that their photoemissivity on a "per area" basis must be substantially larger than that from the Pt substrate. (Note that the large differences in emissivity are not expected to arise from differences in the *vertical* dimension, since the diameter of gold rods is only about 3 times larger than the Pt substrate thickness. In addition, escape depths for low-energy electrons are on the order of a few nanometers, thus presumably attenuating electron emission from regions deep inside the rods.) In fact, the largest S/B ratio for an individual rod, presumably well aligned with the laser polarization, is ∼300 (see Figure 3b). Such a large value implies that the ratio of per area emissivity ε between an aligned Au rod and the Pt substrate is $(\varepsilon_{Au-rod}/\varepsilon_{Pt}) = (S/B)(A_{spot}/A_{rod}) \approx 3 \times 10^5$. In contrast, that ratio for Au pads and the Pt substrate in Figure 2 is only $(\varepsilon_{Au-pad}/\varepsilon_{Pt}) \approx 100$. The corresponding factor of $(\varepsilon_{Au-rod}/\varepsilon_{Pt})/(\varepsilon_{Au-pad}/\varepsilon_{Pt}) \approx 3 \times 10^3$ fold difference between the Au nanorod and Au pad systems is striking. We attribute this large factor to the field enhancement at the nanorod tips (i.e., the well-known lightning-rod effect)[81] and/or to a near-resonant plasmonic enhancement.[82] The possibility of photoemission enhancement due to a plasmon resonance will be investigated in greater detail using wavelength-tunable femtosecond light sources in a separate study.[83]

V. Photoemission Imaging of Silver Nanoparticles

To further demonstrate the sensitivity of scanning multiphoton photoionization microscopy, the photoelectron emission from nanostructures has been studied under conditions where resonant plasmonic enhancement is absent. Specifically, 40 nm diameter silver nanoparticles have been imaged by four-photon photoionization using 840 nm excitation. What makes these particles interesting is that they exhibit a narrow (66 nm FWHM) dipolar plasmon resonance at 413 nm in aqueous solution, without any further strong absorption features in the visible/near-infrared (NIR) range (see Figure 5a). In the substrate/vacuum sample environment probed in these SPIM studies, this plasmon resonance at 413 nm is expected to shift to the blue. Because of low absorbance values, such a blue shift could not be
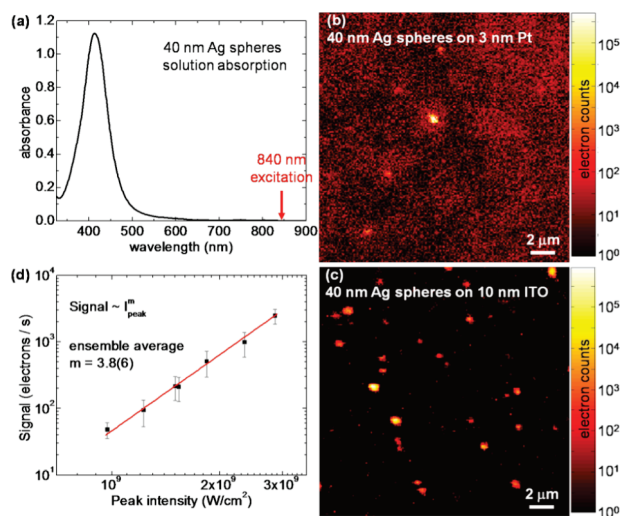
independently confirmed by measuring an ensemble absorption spectrum of Ag spheres spin-coated onto substrates. However, consistent with these expectations, Mie scattering calculations[82] predict a plasmon resonance around 360 nm for 40 nm diameter Ag spheres in vacuum and 380 nm in a medium with a dielectric constant that is between that of vacuum and that of platinum.[84] In any case, excitation at 840 nm is far away from any such plasmonic resonance. Thus, the photoemission process from Ag spheres at this wavelength is not expected to be assisted by the plasmonic field enhancement.

In agreement with expectations, SPIM signals from Ag spheres at 840 nm are consequently quite weak compared to the Au nanorods. Nevertheless, photoelectron emission from individual Ag nanospheres on Pt substrates is sufficiently strong to distinguish these particles from background (Figure 5b) despite the absence of any direct plasmon-resonant enhancement. It is interesting to note that the apparent coverage of Ag spheres determined by SPIM (∼5 spheres in a $20 \times 20 \ \mu m^2$ area) is substantially lower than that observed in the corresponding AFM images (∼20 spheres in a $20 \times 20 \ \mu m^2$ area). In fact, most spheres in Figure 5b are barely distinguishable from the Pt substrate background. Thus, it is likely that a significant fraction of spheres does not produce intense enough photoemission signal to stand out above the background.

We consequently explored the viability of an alternative conductive substrate with a potentially lower photoemissivity, i.e., 10 nm thick ITO films on glass coverslips. Under 800 nm illumination, ITO produces approximately 3 orders of magnitude lower background photoemission signals than the Pt substrate. Indeed, with much lower background, signal from even weakly emitting Ag spheres can now be observed, as shown in Figure 5c, yielding an apparent coverage that is consistent with that determined by AFM. The average signal-to-background ratio for Ag spheres on ITO observed in Figure 5c is $S/B \approx 800$, with some of the brightest spheres even yielding $S/B \approx 10^4$.

Such large signals are obtained despite the fact that 40 nm diameter Ag spheres typically represent only 2.5×10^{-3} of the four-photon excitation spot area.

The photoelectron signal from individual silver spheres follows the expected power dependence on excitation intensity I_{peak} (signal $\sim I_{peak}{}^m$) (Figure 5d). The value of m is observed to vary in the range $3 \leq m \leq 4$ for different spheres, with the ensemble-averaged value (standard deviation) for $N = 14$ particles being $\langle m \rangle = 3.8(6)$. The variability in m for different nanospheres may arise because the work function of silver ranges between 4.2 and 4.8 eV, depending on the crystal facet from which emission occurs and the surface preparation method employed.[85] Thus, photoemission resulting from excitation with 1.47 eV (840 nm) photons may proceed via a third order process for work functions $\Phi < 4.4$ eV and via a fourth order process for $\Phi > 4.4$ eV. In previous work, noninteger power dependence of photoemission intensity, with the exponent varying between 2.9 and 3.7 at different points on the sample, has been observed in an ensemble-measurement study of silver nanoparticles on a silicon substrate upon excitation with $\sim$1.5 eV light.[67] These observations were explained by additional emission pathways coexisting with multiphoton photoemission.

We note that despite the high S/B ratio observed on ITO, silver spheres are about 100 times weaker emitters than gold nanorods on Pt. Qualitatively this is to be expected, given the absence of a nominal plasmonic enhancement in Ag spheres around 840 nm. However, we find it surprising that these Ag spheres are even as strong an electron emitter as experimentally observed. A simple estimate of a nanoparticle's emission strength takes into account three major contributions: (1) the particle's linear absorption cross section at the excitation wavelength, (2) the material's bulk emissivity, and (3) the electric field enhancement due to the nanoparticle geometry, e.g., the "lightning-rod" effect. We next consider these three contributions separately.

First of all, the linear absorption cross section of 40 nm Ag spheres at 840 nm is 40 times smaller than that of Au rods at the same wavelength, i.e. $\sigma_{Ag}/\sigma_{Au} = 1/40$. The excitation probability of an m-plasmon excited state ($m = 4$ for plasmonic processes contributing to four-photon photoemission) should thus scale as the mth power of the probability for a single excitation, i.e., in this case as $(\sigma_{Ag}/\sigma_{Au})^4$.[71] Second, we are unaware of any measurement of bulk four-photon photoemission properties of Ag and Au. However, there is no reason to expect them to be very different in strength. For example, the reported bulk *two-photon* photoemission strengths from flat Ag and Au surfaces are very similar.[86,87] Third, the electric field enhancement for a sphere due to the lightning-rod effect proves to be independent of the particle's radius of curvature. In the dipole approximation, the incident electric field E_0, induces a dipole $d = \alpha E_0$ in the metal particle, where α denotes the particle's polarizability. The induced electric field E_{ind}, in turn, scales as $E_{ind} \sim \alpha E_0 / r^3$, where r is the radial distance from the particle's center. For a particle of size a, $\alpha \approx a^3$; thus, at the particle surface, where photoionization occurs, the induced electric field E_{ind} is independent of the radius a. By combination of the three contributing factors, the ratio of four-photon photoemissive strength from Ag nanospheres and Au nanorods is thus predicted to be $\sim(\sigma_{Ag}/\sigma_{Au})^4 = 10^{-6}$, i.e., 4 orders of magnitude smaller than experimentally observed.

It is worth considering whether this unexpectedly strong photoemission from Ag spheres could arise from an *indirect* plasmonic enhancement, such as from a possible two-photon excitation of the dipolar plasmon resonance. Nonlinear effects,

such as enhanced two-photon fluorescence from nanostructured metals, have been observed.[81,88] In a similar manner, one might speculate that four-photon excitation around 800 nm may benefit from nonlinear enhancements associated with the plasmon resonance (e.g., via two-photon excitation of the plasmon resonance). To test for a possible two-photon excitation of the plasmon resonance, we compared photoemission at two different excitation wavelengths, 760 and 860 nm (data not shown). While there is a roughly 3-fold increase in the overall signal levels for 760 nm vs 860 nm excitation, almost all Ag spheres are clearly visible at both wavelengths. This relative insensitivity to the excitation wavelength rules out any spectrally narrow resonant contribution to photoemission.

V.A. Laser Polarization-Dependence of Photoemission from Ag Spheres. In the absence of either direct or nonlinear plasmonic enhancements, one would predict fairly uniform photoelectron emission strengths from a spin-coated ensemble of Ag spheres. Very much to the contrary, however, Ag spheres on the ITO substrate in Figure 5c exhibit factors of up to a 1000-fold difference in photoelectron emissivity when excited with light of a fixed linear polarization at 840 nm (Figure 7c). To understand these large variations between Ag spheres, we tested for a dependence of their photoemissivity on laser polarization at 840 nm. On the basis of our studies of Au nanorods, one would expect a complete absence of any polarization dependence for these nominally spherical nano-objects. Rather surprisingly, a strongly peaked polarization dependence is observed for almost all spheres. Furthermore, in most cases only a small background signal was detected at a polarization orthogonal to the peak emission, similar to the case of Au nanorods. However, in contrast to Au nanorods, which all consistently produced an $\sim\cos^8(\theta - \theta_0)$ polarization dependence arising from four-photon photoemission from a dipolar source, a much wider variety of phenomena is encountered for Ag spheres. Specifically, while the polarization dependence for many of the brightest Ag spheres is consistent with four-photon photoemission from a dipolar emission source (see Figure 6b), many of the less emissive spheres display a distinctly weaker polarization dependence (see Figure 6c). Photoemission from a few (6 out of 26) spheres, predominantly the most weakly emitting ones, can be observed at all angles, with only a weak polarization-dependent trend on top of a polarization-independent background (see Figure 6d). However, even this surprisingly strong polarization dependence still does not fully explain the observed variations in photoemissivity between different Ag spheres. Indeed, while they exhibit 10^3-fold variation at a fixed laser polarization, the Ag spheres still show a significant 100-fold variation in peak photoemissivities (Figure 7c and Figure 7d). In particular, this contrasts with the much smaller factor of $\sim$10 in variability of the peak photoemission strength observed for gold nanorods (Figure 7b).

The (i) unexpected polarization dependence of photoemission from nominally spherical objects and (ii) large differences in the peak emissivity between Ag nanospheres provoke interesting questions regarding the underlying photoionization mechanism. One explanation that must be considered is the possibility of significant particle aggregation. This is relevant, since such closely spaced particle aggregates could potentially form red-shifted, coupled plasmon resonances in our excitation wavelength range and thus potentially lead to anisotropic photoemission. From multiple SPIM scans, we estimate average coverages of $\sim$20 particles in a 20×20 μm^2 area, which is statistically low enough to ensure single emitting objects per diffraction limited spot. More critically, however, AFM images

Plasmonic Metal Nanostructures

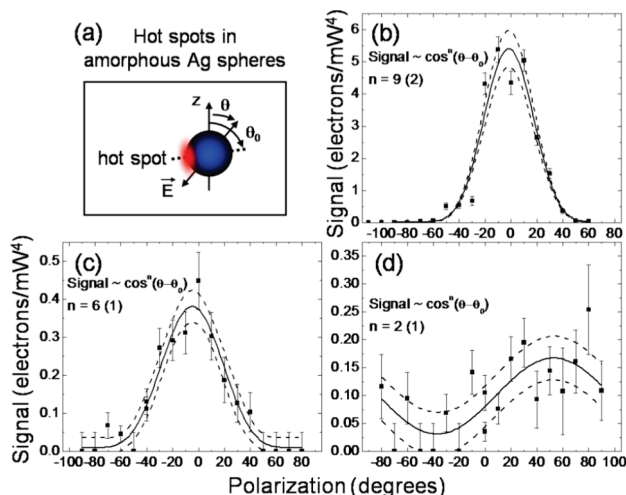*J. Phys. Chem. C, Vol. 115, No. 1, 2011* **89**

Figure 6. Many nominally spherical silver nanoparticles exhibit strong polarization dependent photoionization yield. (a) Such anisotropy, for example, could be associated with variations in electron emissivity of the different crystal facets that are exposed in the polycrystalline particles, as well as possible localized electric field hot spots at grain boundaries and microscopic structural defects. (b) The brightest spheres show a strong polarization-dependent behavior, consistent with a four-photon photoemission from a dipolar emission source. (c) More weakly emitting nanospheres tend to exhibit less pronounced polarization-dependent behavior. (d) Some of the weakest-emitting spheres display almost no polarization dependence. Dashed lines mark limits for 90% confidence levels.
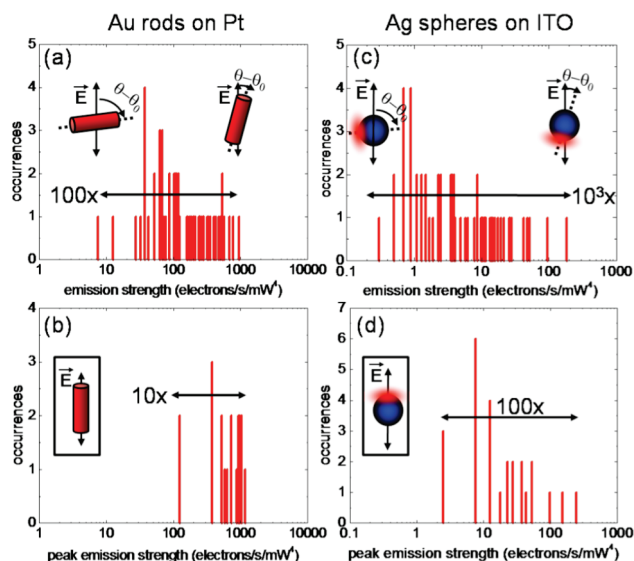

Figure 7. Distributions in photoemission strength from (a, b) single Au rods on Pt and (c, d) Ag spheres on ITO. (a, c) Distribution of photoemissivity at a fixed linear polarization. Bright (weak) emitters presumably have their long axis, or a local hot spot, aligned with (orthogonal to) the laser polarization. (b, d) Distributions of the *peak* photoemissivity, i.e., emissivity value at the peak of each particle's polarization dependence, are much narrower than in (a) and (c). Ag spheres represent a much more heterogeneous sample (100× peak emissivity variation) than Au rods (10× variation).

of identically prepared samples reveal coverages that are consistent with those observed in SPIM images, indicating that essentially all spheres exhibit detectable electron emission. If the observed photoemission signal originated only from aggregates, in contrast one would expect significantly lower apparent coverage in SPIM.

Another possible interpretation of our data is that multiphoton photoemission from solution-synthesized, *polycrystalline,* silver
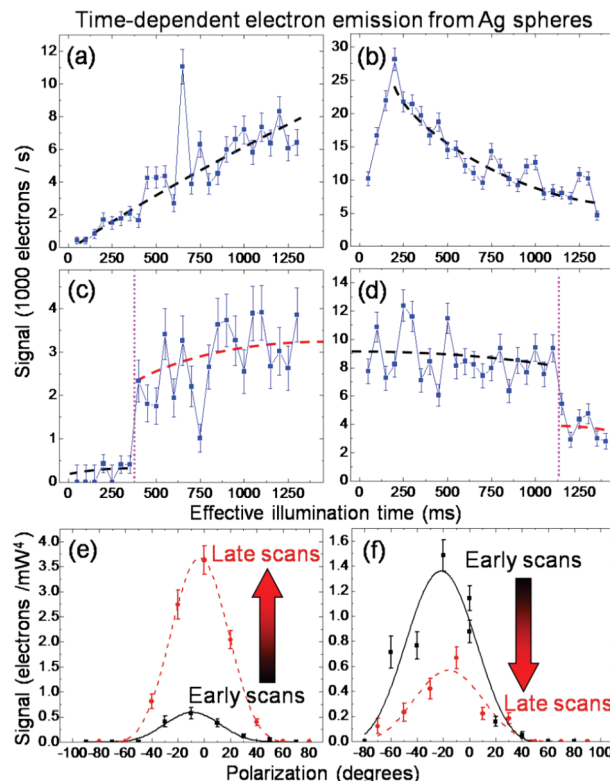

Figure 8. (a–d) Time sequences of the emission from individual Ag spheres recorded by repeatedly scanning the same sample area. Emission from individual spheres is plotted vs the time that each sphere spends under illumination (~50 ms per scan). Emission from single particles may gradually (a) increase with time, exhibit sudden spikes, or (b) decrease gradually (dashed lines serve to guide the eye). (c) Abrupt increases or (d) decreases between more or less constant initial and final emission intensity are observed. (e, f) Before and after such jumps, the polarization dependence is found to remain approximately unchanged ["early scans" and "late scans" in (e) and (f)]. For (a–d) the excitation intensity was 1.9×10^9 W/cm^2, while for (e) and (f) it was 3.6×10^9 W/cm^2.

spheres is dominated by strong local variations in photoemission propensity arising from the microscopic features in their structure. For example, such local variations could be a consequence of the different work functions associated with the various crystal facets in the nanoparticle. Alternatively, localized regions of strong electric fields that may be expected near grain boundaries and structural defects in these polycrystalline particles could give rise to locally enhanced photoemissivity. Related effects have been observed in recent experiments on *evaporated* metal nanostructures. For example, strongly polarization-dependent electron emission has been detected from 140 nm Pb clusters on a silicon substrate.[73] Furthermore, recent observations of locations of strongly enhanced electron emission on evaporated silver gratings[25] and lithographically patterned silver nanodisks[89] have all been tentatively explained by local electric field hot spots.

V.B. Temporal Fluctuations in the Photoelectron Emission from Ag Spheres. Additional important information regarding the photoemission mechanism comes from the surprising observation that the electron signals from individual Ag spheres, in contrast to Au rods, are time-dependent. In Figure 8, the photoemission signal from a few representative individual spheres in a sequence of scans under identical excitation conditions is shown. Photoemission signals are observed to rise or decay with time, as shown in Figure 8a and Figure 8b, respectively. Transient spikes or dips are occasionally encoun-

90 *J. Phys. Chem. C, Vol. 115, No. 1, 2011*

Schweikhard et al.

tered as well. Furthermore, some spheres exhibit abrupt jumps between more or less constant initial and final emission levels, as shown in Figure 8c and Figure 8d. In contrast, such striking time-dependence was not observed for any of the studied gold rods. Interestingly, measurements of the polarization dependence of photoemission from Ag spheres prior and after abrupt jumps in signal levels suggest that these jumps are not accompanied by drastic changes in the polarization angle at which peak emission occurs (see Figure 8e and Figure 8f).

Both the observed anisotropies and the temporal variations in photoemission appear to suggest that photoemission is strongly influenced by microscopic structural features in these polycrystalline particles rather than being driven by the lowest-order dipolar electron oscillation. These microscopic features may be very sensitive to small light-induced structural rearrangements, as has been observed by Jin and co-workers[8] in the conversion of silver nanospheres to nanoprisms, which could explain the observed dramatic time-dependent signals. A more detailed study of the photoemission mechanism of *individual* Ag nanospheres (as opposed to particle aggregates) is clearly worthwhile but is beyond the scope of the current work.

VI. Summary and Conclusions

We have demonstrated that scanning multiphoton photoionization microscopy is a viable technique for single-particle studies of heterogeneous samples of colloidal metal nanoparticles as well as photolithographically fabricated metal nanostructures. Four-photon photoemission from Au nanorods on Pt substrate was studied under 840 nm excitation. Individual nanoparticles exhibit strong $\cos^8(\theta - \theta_0)$ dependence of photoemission strength on the angle between laser polarization (θ) and the rod axis (θ_0), suggesting that four-photon photoemission is initiated by excitation of the long-axis dipolar plasmon resonance. For on-axis excitation, the photoemission strengths of different rods vary less than 10-fold. Such a small factor is remarkable given the fourth order photoemission dependence on local electric field strength surrounding the emitter, thus suggesting a relatively high degree of homogeneity among the Au nanorods.

Moreover, four-photon photoemission from polycrystalline Ag nanospheres on both Pt and ITO substrates have also been studied under 840 nm excitation. Surprisingly, strongly polarization-dependent photoelectron signals are also observed for these nominally spherical particles. However, different particles exhibit very different degrees of anisotropy with some showing strongly polarization-dependent behavior akin to the one observed in case of Au nanorods, whereas others exhibit almost none. Just as surprisingly, the observed photoelectron signals from Ag spheres, in contrast to Au rods, display striking time-dependence. More work is clearly necessary to elucidate the precise mechanisms underlying these observations.

The results suggest that the image contrast in SPIM can arise from a variety of different mechanisms, i.e., intrinsic differences in the strength of photoemission from different chemical species, photoemission enhancements due to plasmon resonances, and lightning-rod effects associated with concentrated electric fields near nanoscale structural features. Single-particle studies of polarization-, intensity-, excitation-wavelength-, and even time-dependence of photoemission signals provide powerful means to unravel the contributions of these different mechanisms, even in strongly heterogeneous samples of particles. These studies thus establish the SPIM technique as a valuable, new approach to the study of local electronic properties of individual metallic nanostructures.

References and Notes

(1) Yin, Y.; Alivisatos, A. P. *Nature* **2005**, *437*, 664–670.
(2) Choi, C. L.; Alivisatos, A. P. *Annu. Rev. Phys. Chem.* **2010**, *61*, 369–389.
(3) Pelton, M.; Aizpurua, J.; Bryant, G. *Laser Photonics Rev.* **2008**, *2* (3), 136–159.
(4) Alekseeva, A. V.; Bogatyrev, V. A.; Khlebtsov, B. N.; Mel'nikov, A. G.; Dykman, L. A.; Khlebtsov, N. G. *Colloid J.* **2006**, *68*, 661–678.
(5) Murphy, C. J.; San, T. K.; Gole, A. M.; Orendorff, C. J.; Gao, J. X.; Gou, L.; Hunyadi, S. E.; Li, T. *J. Phys. Chem. B* **2005**, *109* (29), 13857–13870.
(6) Sun, Y.; Xia, Y. *Science* **2002**, *298* (5601), 2176–2179.
(7) Maillard, M.; Giorgio, S.; Pileni, M. P. *Adv. Mater.* **2002**, *14* (15), 1084–1086.
(8) Jin, R.; Cao, Y.; Mirkin, C. A.; Kelly, K. L.; Schatz, G. C.; Zheng, J. G. *Science* **2001**, *294* (5548), 1901–1903.
(9) Brus, L. *Acc. Chem. Res.* **2008**, *41* (12), 1742–1749.
(10) Haes, A. J.; Haynes, C. L.; McFarland, A. D.; Schatz, G. C.; Van Duyne, R. R.; Zou, S. L. *MRS Bull.* **2005**, *30* (5), 368–375.
(11) Halas, N. J. *MRS Bull.* **2005**, *30*, 362–367.
(12) Callegari, A.; Tonti, D.; Chergui, M. *Nano Lett.* **2003**, *3* (11), 1565–1568.
(13) Seo, W. S.; Kim, S. M.; Kim, Y.-M.; Sun, X.; Dai, H. *Small* **2008**, *4*, 1968–1971.
(14) Sun, S.; Zeng, H.; Robinson, D. B.; Raoux, S.; Rice, P. M.; Wang, S. X. *J. Am. Chem. Soc.* **2004**, *126*, 273–279.
(15) Watanabe, K.; Menzel, D.; Nilius, N.; Freund, H. J. *Chem. Rev.* **2006**, *106*, 4301–4320.
(16) Somorjai, G. A.; York, R. L.; Butcher, D.; Park, J. Y. *Phys. Chem. Chem. Phys.* **2007**, *9* (27), 3500–3513.
(17) Pillai, S.; Catchpole, K. R.; Trupke, T.; Green, M. A. *J. Appl. Phys.* **2007**, *101*, 093105.
(18) Anker, J. N.; Hall, W. P.; Lyandres, O.; Shah, N. C.; Zhao, J.; Van Duyne, R. P. *Nat. Mater.* **2008**, *7* (6), 442.
(19) Konstantatos, G.; Sargent, E. H. *Nat. Nanotechnol.* **2010**, *5* (6), 391.
(20) Chen, W.; Zhang, J. Z.; Joly, A. G. *J. Nanosci. Nanotechnol.* **2004**, *4* (8), 919–947.
(21) Barnes, W. L.; Dereux, A.; Ebbesen, T. W. *Nature* **2003**, *424*, 824–830.
(22) Ozbay, E. *Science* **2006**, *311* (5758), 189–193.
(23) Rosi, N. L.; Mirkin, C. A. *Chem. Rev.* **2005**, *105*, 1547–1562.
(24) Mohamed, M. B.; Volkov, V.; Link, S.; El-Sayed, M. A. *Chem. Phys. Lett.* **2000**, *317* (6), 517.
(25) Kubo, A.; Onda, K.; Petek, H.; Sun, Z.; Jung, Y. S.; Kim, H. K. *Nano Lett.* **2005**, *5* (6), 1123–1127.
(26) Kubo, A.; Jung, Y. S.; Kim, H. K.; Petek, H. *J. Phys. B: At. Mol. Opt. Phys.* **2007**, *40* (11), S259–S272.
(27) Kubo, A.; Pontius, N.; Petek, H. *Nano Lett.* **2007**, *7* (2), 470–475.
(28) Kubo, A.; Onda, K.; Petek, H.; Sun, Z. J.; Jung, Y. S.; Kim, H. K. *Nano Lett.* **2005**, *5* (6), 1123–1127.
(29) Kelly, K. L.; Coronado, E.; Zhao, L. L.; Schatz, G. C. *J. Phys. Chem. B* **2003**, *107*, 668–677.
(30) Kreibig, U., Vollmer, M., Eds. *Optical Properties of Metal Clusters*; Springer Series in Materials Science, Vol. 25; Springer-Verlag: Heidelberg, 1995; p 532.
(31) Mock, J. J.; Barbic, M.; Smith, D. R.; Schultz, D. A.; Schultz, S. *J. Chem. Phys.* **2002**, *116* (15), 6755–6759.
(32) Willets, K. A.; Van Duyne, R. P. *Annu. Rev. Phys. Chem.* **2007**, *58*, 267–297.
(33) Xia, Y. N.; Halas, N. J. *MRS Bull.* **2005**, *30* (5), 338–344.
(34) West, J. L.; Halas, N. J. *Annu. Rev. Biomed. Eng.* **2003**, *5*, 285–292.
(35) Link, S.; El-Sayed, M. A. *Int. Rev. Phys. Chem.* **2000**, *19* (3), 409–453.
(36) Bardhan, R.; Grady, N. K.; Cole, J. R.; Joshi, A.; Halas, N. J. *ACS Nano* **2009**, *3*, 744–752.
(37) Prodan, E.; Radloff, C.; Halas, N. J.; Nordlander, P. *Science* **2003**, *302* (5644), 419–422.
(38) McFarland, A. D.; Van Duyne, R. P. *Nano Lett.* **2003**, *3* (8), 1057–1062.
(39) Sherry, L. J.; Chang, S. H.; Schatz, G. C.; Van Duyne, R. P.; Wiley, B. J.; Xia, Y. N. *Nano Lett.* **2005**, *5* (10), 2034–2038.
(40) Moerner, W. E. *Science* **1994**, *265* (5168), 46–53.

(41) Nirmal, M.; Dabbousi, B. O.; Bawendi, M. G.; Macklin, J. J.; Trautman, J. K.; Harris, T. D.; Brus, L. E. *Nature* **1996**, *383*, 802–804.

(42) Kuno, M.; Fromm, D. P.; Hamann, H. F.; Gallagher, A.; Nesbitt, D. J. *J. Chem. Phys.* **2001**, *115*, 1028–1040.

(43) Frantsuzov, P.; Kuno, M.; Janko, B.; Marcus, R. A. *Nat. Phys.* **2008**, *4*, 519–522.

(44) Shaevitz, J. W.; Block, S. M.; Schnitzer, M. J. *Biophys. J.* **2005**, *89*, 2277–2285.

(45) Moerner, W. E.; Fromm, D. P. *Rev. Sci. Instrum.* **2003**, *74*, 3597–3619.

(46) Sönnichsen, C.; Franzl, T.; Wilk, T.; von Plessen, G.; Feldmann, J.; Wilson, O.; Mulvaney, P. *Phys. Rev. Lett.* **2002**, *88* (7), 077402.

(47) Novo, C.; Funston, A. M.; Mulvaney, P. *Nat. Nanotechnol.* **2008**, *3* (10), 598.

(48) Nie, S.; Emery, S. R. *Science* **1997**, *275*, 1102.

(49) Muskens, O. L.; Bachelier, G.; Fatti, N. D.; Vallee, F.; Brioude, A.; Jiang, X.; Pileni, M.-P. *J. Phys. Chem. C* **2008**, *112* (24), 8917.

(50) Muskens, O. L.; Billaud, P.; Broyer, M.; Fatti, N. D.; Vallée, F. *Phys. Rev. B* **2008**, *78* (20), 205410.

(51) Billaud, P.; Marhaba, S.; Grillet, N.; Cottancin, E.; Bonnet, C.; Lermé, J.; Vialle, J.-L.; Broyer, M.; Pellarin, M. *Rev. Sci. Instrum.* **2010**, *81*, 043101.

(52) Yildiz, A.; Selvin, P. R. *Acc. Chem. Res.* **2005**, *38* (7), 574–582.

(53) Lacoste, T. D.; Michalet, X.; Pinaud, F.; Chemla, D. S.; Alivisatos, A. P.; Weiss, S. *Proc. Natl. Acad. Sci. U.S.A.* **2000**, *97* (17), 9461–9466.

(54) Betzig, E.; Patterson, G. H.; Sougrat, R.; Lindwasser, O. W.; Olenych, S.; Bonifacino, J. S.; Davidson, M. W.; Lippincott-Schwartz, J.; Hess, H. F. *Science* **2006**, *313* (5793), 1642–1645.

(55) Rust, M. J.; Bates, M.; Zhuang, X. *Nat. Methods* **2006**, *3*, 793–795.

(56) Hess, S. T.; Girirajan, T. P. K.; Mason, M. D. *Biophys. J.* **2006**, *91*, 4258–4272.

(57) Hell, S. W.; Wichmann, J. *Opt. Lett.* **1994**, *19* (11), 780–782.

(58) Lord, S. J.; Lee, H. D.; Moerner, W. E. *Anal. Chem.* **2010**, *82*, 2192–2203.

(59) Kohei, I.; Tetsuhiko, N.; Hiromi, O. *J. Chem. Phys.* **2005**, *122* (15), 154701.

(60) Axelrod, D. *Methods Cell Biol.* **2008**, *89*, 169–221.

(61) Hamann, H. F.; Gallagher, A.; Nesbitt, D. J. *Appl. Phys. Lett.* **1998**, *73* (11), 1469–1471.

(62) Farahani, J.; Eisler, H.-J.; Pohl, D. W.; Hecht, B. *Phys. Rev. Lett.* **2005**, *95*, 017402.

(63) Fort, E.; Gresillon, S. *J. Phys. D: Appl. Phys.* **2008**, *41*, 013001.

(64) Zhao, J.; Pontius, N.; Winkelmann, A.; Sametoglu, V.; Kubo, A.; Borisov, A. G.; Sanchez-Portal, D.; Silkin, V. M.; Chulkov, E. V.; Echenique, P.; Petek, H. *Phys. Rev. B* **2008**, *78*, 085419.

(65) Evers, F.; Rakete, C.; Watanabe, K.; Menzel, D.; Freund, H. J. *Surf. Sci.* **2005**, *593*, 43–48.

(66) Pfeiffer, W.; Kennerknecht, C.; Merschdorf, M. *Appl. Phys. A: Mater. Sci. Process.* **2004**, *78*, 1011–1028.

(67) Gloskovskii, A.; Valdaitsev, D.; Nepijko, S. A.; Schoenhense, G.; Rethfeld, B. *Surf. Sci.* **2007**, *601*, 4706–4713.

(68) Kennerknecht, C.; Hövel, H.; Merschdorf, M.; Voll, S.; Pfeiffer, W. *Appl. Phys. B: Lasers Opt.* **2001**, *73* (4), 425–429.

(69) Merschdorf, M.; Pfeiffer, W.; Thon, A.; Voll, S.; Gerber, G. *Appl. Phys. A: Mater. Sci. Process.* **2000**, *71* (5), 547–552.

(70) Bauer, M.; Wiemann, C.; Lange, J.; Bayer, D.; Rohmer, M.; Aeschlimann, M. *Appl. Phys. A: Mater. Sci. Process.* **2007**, *88* (3), 473–480.

(71) Lehmann, J.; Merschdorf, M.; Pfeiffer, W.; Thon, A.; Voll, S.; Gerber, G. *Phys. Rev. Lett.* **2000**, *85*, 2921–2924.

(72) Munakata, T.; Masuda, T.; Ueno, N.; Sakaya, S.; Sugiyama, T.; Takehiro, N.; Sonoda, Y. *Surf. Sci.* **2003**, *532−535*, 1140–1144.

(73) Fecher, G. H.; Schmidt, O.; Hwu, Y.; Schonhense, G. *J. Electron Spectrosc. Relat. Phenom.* **2002**, *126*, 77–87.

(74) Monti, O. L. A.; Baker, T. A.; Nesbitt, D. J. *J. Chem. Phys.* **2006**, *125*, 154709.

(75) Rohmer, M.; Bauer, M.; Leissner, T.; Schneider, C.; Fischer, A.; Niedner-Schatteburg, G.; Issendorff, B. v.; Aeschlimann, M. *Phys. Status Solidi B* **2010**, *247* (5), 1132–1138.

(76) Stockman, M. I.; Kling, M. F.; Kleineberg, U.; Krausz, F. *Nat. Photonics* **2007**, *1*, 539–544.

(77) Douillard, L.; Charra, F.; Korczak, Z.; Bachelot, R.; Kostcheev, S.; Lerondel, G.; Adam, P.-M.; Royer, P. *Nano Lett.* **2008**, *8* (3), 935.

(78) Word, R. C.; Dornan, T.; Könenkamp, R. *Appl. Phys. Lett.* **2010**, *96*, 251110.

(79) Cinchetti, M.; Gloskovskii, A.; Nepijko, S. A.; Schoenhense, G.; Rochholz, H.; Kreiter, M. *Phys. Rev. Lett.* **2005**, *95*, 047601.

(80) We note that mention of commercial product names is for information only; it does not imply National Institute of Standards and Technology recommendation or endorsement, nor does it imply that products mentioned are necessarily the best available for the purpose.

(81) Boyd, G. T.; Yu, Z. H.; Shen, Y. R. *Phys. Rev. Lett.* **1986**, *33*, 7923–7935.

(82) Bohren, C. F.; Huffman, D. R. *Absorption and Scattering of Light by Small Particles*; Wiley VCH: Weinheim, Germany, 1983.

(83) Schweikhard, V.; Baker, T. A.; Nesbitt, D. J. Manuscript in preparation.

(84) Xu, G.; Chen, Y.; Tazawa, M.; Jin, P. *Appl. Phys. Lett.* **2006**, *88*, 043114.

(85) Chelvayohan, M.; Mee, C. H. B. *J. Phys. C: Solid State Phys.* **1982**, *15* (10), 2305–2312.

(86) Stuckless, J. T.; Moskovits, M. *Phys. Rev. B* **1989**, *40*, 9997–9998.

(87) Sohn, Y.; Richter, J.; Ament, J.; Stuckless, J. T. *Appl. Phys. Lett.* **2004**, *84*, 76–78.

(88) Schuck, P. J.; Fromm, D. P.; Sundaramurthy, A.; Kino, G. S.; Moerner, W. E. *Phys. Rev. Lett.* **2005**, *94* (1), 017402.

(89) Wiemann, C.; Bayer, D.; Rohmer, M.; Aeschlimann, M.; Bauer, M. *Surf. Sci.* **2007**, *601*, 4714–4721.